The Journal of Experimental Biology **199**, 1133–1146 (1996)
Printed in Great Britain © The Company of Biologists Limited 1996
JEB0229

STRAIN-RATE-DEPENDENT MECHANICAL PROPERTIES OF THE EQUINE HOOF WALL

MARIO A. KASAPI AND JOHN M. GOSLINE

Department of Zoology, University of British Columbia, 6270 University Boulevard, Vancouver, BC, Canada V6T 1Z4

Accepted 30 January 1996

Summary

The mechanical properties of fully hydrated equine hoof wall were examined at various loading rates in compact tension (CT) fracture, tensile and three-point bending dynamic tests to determine possible effects of hoof wall viscoelasticity on fracture toughness and tensile parameters. Four cross-head rates were used in CT tests: 1.7×10^{-5}, 1.7×10^{-3}, 1.7×10^{-2} and $2.5\,m\,s^{-1}$; four strain rates were used in tensile tests: 1.6×10^{-3}, 3.2×10^{-2}, 0.33 and $70\,s^{-1}$. Speeds for the highest test rates were achieved using a large, custom-built impact pendulum. Bending test frequencies ranged from 0.04 to 200 Hz.

In CT tests, both the initial modulus E_i and the stress intensity factor K rose with increasing strain rate (from 0.38 to 0.76 GPa for E_i and from 0.71 to $1.4\,MN\,m^{-3/2}$ for K), whereas the fracture toughness parameter J remained constant at $12\,kJ\,m^{-2}$. All tensile parameters except ultimate strain were sensitive to strain rate. E_i, total energy to breakage and maximum stress rose with increasing strain rate from 0.28 to 0.85 GPa, from 5.4 to $9.7\,MJ\,m^{-3}$ and from 17 to 31 MPa, respectively. Data from low-amplitude dynamic tests agreed well with E_i trends from CT and tensile tests.

Direction of crack growth differed through the thickness of the wall, the pattern of which resembled a trilaminar ply. Although scanning electron microscopic examination of fracture surfaces revealed a decreasing pseudo-ductile behaviour with increasing strain rate, and ultimate tensile parameters are positively affected, equine hoof wall viscoelasticity does not appear to compromise fracture toughness at high strain rates.

Key words: strain rate, mechanical properties, equine, hoof wall, *Equus caballus*.

Introduction

Most biological materials are neither purely elastic nor purely viscous in mechanical behaviour; instead, they show a combination of both and are hence termed viscoelastic. A consequence of viscoelasticity is mechanical strain rate sensitivity and a possible transition from ductile or pseudo-ductile to brittle behaviour, suggesting a drop in fracture toughness with increasing strain rate. Hydration-dependence of fracture toughness of hoof wall (Bertram and Gosline, 1987) is one manifestation of viscoelasticity and suggests the possibility for brittle failure of equine hoof wall at high strain rates. Reduced toughness could have serious implications to the horse since, as with most structural biomaterials, loading conditions are rarely static. Increased hoof wall loading rate is concomitant with an increase in animal speed; strain rates on the surface of equine hoof wall have been shown to vary between 0.02 and $1.7\,s^{-1}$ for a horse travelling at 1–6 $m\,s^{-1}$ (Thomason *et al.* 1992). Localized stress concentrations, which may result from impact onto an uneven substratum such as a rocky surface, are coupled with localized strain rates which will greatly exceed those observed on the surface of the wall. Failure may lead to infection and subsequent death of the animal.

The equine hoof wall resembles an obliquely truncated cone (see Fig. 1A), forming the outer load-bearing surface of the foot and suspending the bony skeleton *via* collagen fibres. It is composed of epidermal cells filled with a protein-based fibre-reinforced molecular composite called α-keratin (see Fig. 1B). The fundamental units of the fibrous phase are 7–8 nm diameter intermediate filaments (IFs). IFs are composed of substructures organized like a two-stranded protein rope, or protofibril, each strand of the rope represented by an α-helix (see Steinert *et al.* 1993). Protofibrils appear to form tetrameric unit structures of paired rope molecules; an undetermined number of these tetramers are organized concentrically and supercoil to form unidirectionally organized IF molecules (see Fig. 1C) which lie in the plane of cells. Interspersed between IF molecules are globular matrix proteins. Cell adhesion appears to be achieved with desmosomes and septate-like junctions (Leach, 1993); it may also be facilitated by a glycoprotein ‘glue’, as in mammalian epidermis (Matoltsy,

1975) and a high degree of plasma membrane interdigitation (see Leach, 1980). Similar to the organization of keratinized cells in rhinoceros horn (Makinson, 1954; Ryder, 1962), cells of the stratum medium (SM; middle region and bulk of the hoof wall, see Fig. 1A) are arranged into one of two patterns: 200–300 μm diameter hollow tubules that run the length of the hoof or an intertubular cellular matrix which lies at large angles relative to the long axis of tubules (Fig. 1).

Although equine hoof wall is loaded primarily in compression (Thomason *et al.* 1992), hoof tissue probably ultimately fails in tension. Tensile properties are therefore of primary interest when evaluating hoof performance. Fracture mechanics is important because, although the total energy input to a material may appear sufficient to characterise the toughness of a material, it provides no information about the behaviour of a material with a crack or a flaw. Linear elastic fracture mechanics (LEFM; see Broek, 1982) attempts to quantify the fracture toughness of a material given the knowledge of a few mechanical parameters generated from simple tests. One toughness parameter attainable from LEFM is the strain energy release rate G. This parameter represents the strain energy released per unit length of crack growth and was developed for linear elastic materials where all energy released during crack propagation equals the surface energy of the newly formed surface. In many materials, however, energy is absorbed by crack tip plasticity (permanent deformation of the material at the crack tip) as well as by the formation of new surfaces during crack propagation. For materials in which plasticity effects are significant, the J-integral technique provides a more accurate measure of toughness. J is a measure of the change in energy per unit change in crack length (Rice, 1968). In purely elastic materials, G and J are equal.

The stress intensity factor K is another measure of fracture toughness and was developed to represent the highest stress intensity that a material can withstand in the presence of a crack. Although K is another parameter of LEFM, it may provide useful information in elastic-plastic materials and has been used to represent the fracture toughness of bone (e.g. Behiri and Bonfield, 1984, 1989; Bonfield, 1987) and the middle region of the SM of equine hoof wall (Bertram, 1984).

Although the mechanical effects of hoof viscoelasticity with loading rate may have significant consequences for the animal, they are still unknown. In addition, the mechanical behaviour of the entire thickness of hoof SM tissue has not yet been evaluated. In this study, we quantify fracture and tensile parameters of hoof tissue encompassing the entire SM at full hydration and conclude that, although the hoof wall shows strain-rate tensile properties, fracture toughness is not compromised over the range of strain rates anticipated *in vivo*.

Materials and methods

Hooves from nine horses (*Equus caballus* L.) were used in this study. Whole feet from horses of variable age and unknown physical condition were obtained from a local (Aldegrove, BC, Canada) slaughterhouse within a few days of death of the animal (animals were destroyed for reasons other than this study) and were disinfected in 0.02 % benzalkonium chloride in distilled water for about 1 h before use. SM tissue from the toe region of the hoof wall was isolated using a band saw, and only this region was used in the study. Hoof wall tissue was then separated from the third phalanx (coffin bone) using a scalpel. Wall material in direct contact with the ground is mechanically inferior to the rest of the hoof (Bertram, 1984); therefore, the distal-most 1 cm was discarded. The proximal-most 1 cm was also discarded as this area contains tubule-forming dermal papillae. Three types of test specimen were produced from wall material: compact tension (CT), tensile and dynamic specimens (Fig. 1).

CT specimens

Hoof wall material from six horses were shaped into 35 CT specimens using a thin sectioning machine (Gillings-Hamco) which had been modified to act as a grinder by adhering waterproof sandpaper (Diamond Grit 180) onto a cutting wheel. A constant flow of tap water kept specimens cool and hydrated during the shaping process. Inner and outer portions of the wall were also ground smooth, removing the stratum internum (SI; innermost, lamellar region of the hoof wall) and stratum externum (SE; outermost, thin layer of the wall); the gradual curvature of the wall at this region of the foot allowed flattening of these surfaces with minimal loss of SM tissue. Although a slight variability in specimen dimensions was unavoidable, all sides were parallel. Holes for clevis pins were made using a Maximat7 drill press. Specimen shape (Fig. 1F) followed ASTM (E813-89) guidelines for fracture toughness testing as closely as possible; however, the morphology of the foot made some modifications unavoidable. Although specimen thickness was occasionally less than that recommended, the full thickness of the SM was used (9.8±1.7 mm; pooled mean ±1 S.D.). To simulate an *in situ* fracture condition to which the hoof may be regularly exposed, CT pieces were notched parallel to the longitudinal axis of the tubules and across the wall thickness using a band saw (0.6 mm thick blade), and the notch front was sharpened using a single-edge razorblade with the aid of an attachment to the drill press. The graphical method used to determine the fracture toughness parameter J was adapted from Landes and Begley (1971) and required that a number of specimens be produced with varying initial notch lengths. After preliminary testing, it was decided that only specimens with notch length (a) to specimen width (W) ratios below 0.65 could be used to determine J, because the stress field at the notch front of specimens with a/W ratios greater than this was thought to be influenced by the end of the sample.

Completed specimens were hydrated in distilled water (with 0.02 % sodium azide to prevent bacterial growth) at 4 °C for at least 7 days. Testing was performed at full hydration after allowing specimens to equilibrate for 24 h at room temperature (approximately 20 °C). Specimens obtained from each horse were equally divided between experimental groups.

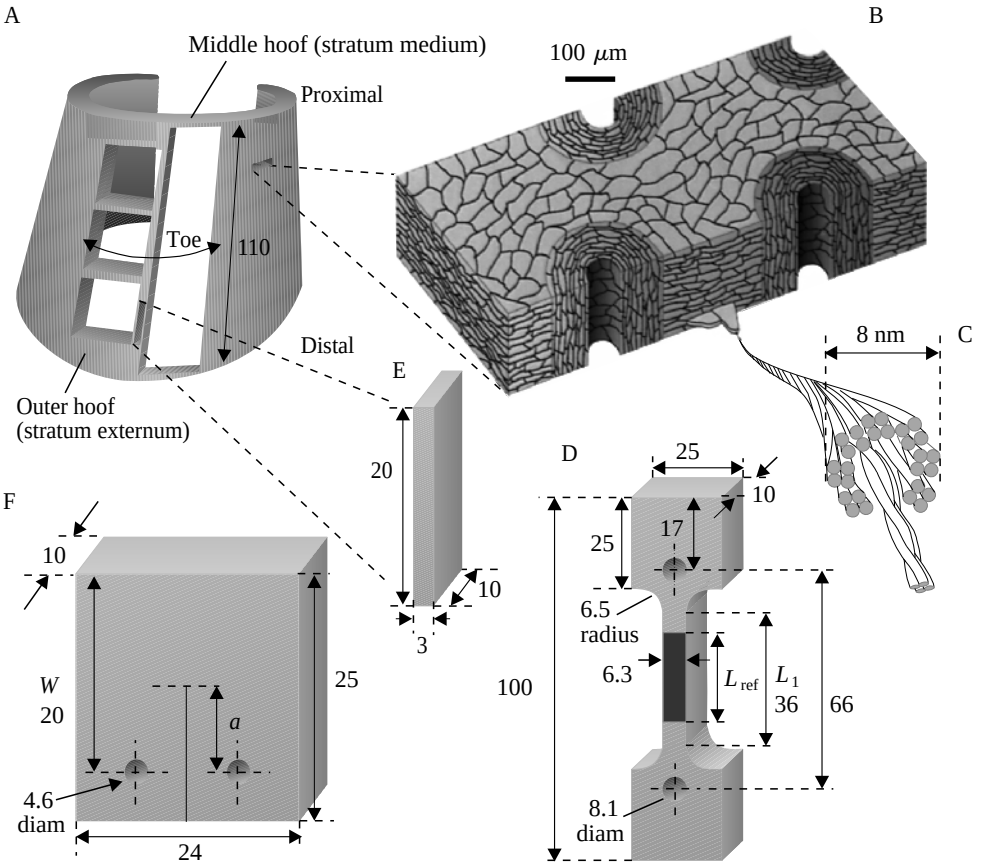

Fig. 1. (A) Front view of the equine hoof wall showing example positions from where samples were obtained; (B) sketch of a hoof wall sample showing cells forming tubules and intertubular matrix (after Bertram and Gosline, 1986); (C) a keratin intermediate filament, showing the concentric association of tetrameric α-helices; (D) tensile specimen (showing the VDA tracking segment or reference bar); (E) dynamic specimen; (F) CT specimen. All dimensions are approximate and in millimetres unless otherwise indicated. *a*, notch length; *W*, specimen width; L_{ref}, reference bar; L_1, parallel segment.

Tensile specimens

Eight hooves from two horses provided material for 16 tensile specimens. Each experimental group received two specimens from each horse (one from a forelimb and one from a hindlimb). Tensile specimen morphology (Fig. 1D) was based on dimensions recommended by ASTM (E8M-90a); however, since the length of hoof columns was limited by the size of the hoof, the overall length was often less than that suggested. Specimen thickness was greater than that recommended in order to include the entire thickness of the SM. To produce specimens of uniform shape, an aluminium template was clamped to a hoof column and the sample milled to shape. Holes for the loading pins were then drilled in appropriate positions. Inner and outer surfaces of the test specimens were carefully ground with the modified Gillings-Hamco apparatus, removing the SI, the SE and any minor surface irregularities and flaws. A reference bar was drawn on the inner hoof face of each sample with a black wax pencil to act as a strain reference during the experiment. Completed specimens were hydrated in distilled water with 0.02 % sodium azide at 4 °C for at least 5 days. Testing was performed at full hydration after allowing specimens to equilibrate for 24 h at room temperature.

Dynamic three-point bending specimens

Two three-point bending dynamic test samples were obtained from different animals. Hoof strips were cut using the thin sectioning machine and then cut to the appropriate width and length (Fig. 1E) using a single-edge razorblade. Beams measured approximately 3 mm×10 mm×20 mm and included material from the entire thickness of the SM.

Test protocol and data analysis

Slower strain rate experiments employed an Instron testing machine (model 1122) with a 500 kg load cell. The cross-head speed was limited to 1.7×10^{-2} m s^{-1}; therefore, a large (3.15 m total height) pendulum was constructed to determine mechanical properties at higher strain rates (impact). Four cross-head rates were used in each test type: 1.7×10^{-5}, 1.7×10^{-3}, 1.7×10^{-2} and 2.5±0.3 m s^{-1} (mean ±1 S.D.) for CT tests, 8.3×10^{-5}, 1.7×10^{-3}, 1.7×10^{-2} and 3.9±0.4 m s^{-1} (mean ±1 S.D.) for tensile tests [corresponding to tensile strain rates, $\dot{\epsilon}$, of $1.6\times10^{-3}\pm0.2\times10^{-3}$, $3.2\times10^{-2}\pm0.5\times10^{-2}$, 0.33±0.04 and 70±5 s^{-1} (mean ±1 S.D.), respectively]. Although the strain rates recorded by Thomason *et al.* (1992) encompassed a more limited range, our test range was believed to encompass the range of strain rates to which an animal may subject the hoof, including local rates experienced at the ground contact surface and at a crack front during high-speed locomotion.

CT tests

Instron fracture tests were conducted in mode I crack mouth opening (see Broek, 1988) in distilled water using the clevis

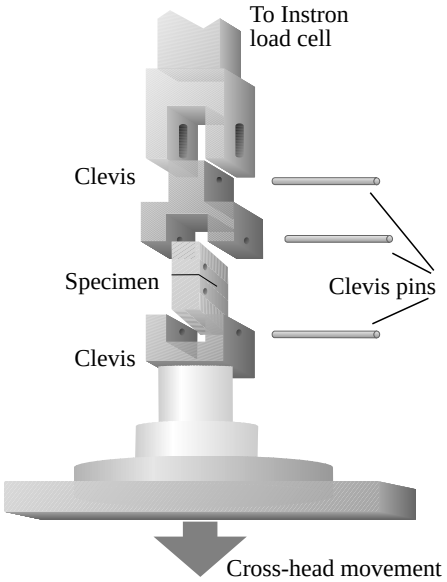

Fig. 2. Exploded diagram of the clevis loading system with a CT specimen. Specimens were anchored to the load cell at the top of the Instron; cross-head movement is downwards. Buffer slots in the upper clevis allowed the cross-head to reach speed before load was applied to the specimen. The use of pins allowed realignment of components during an experiment.

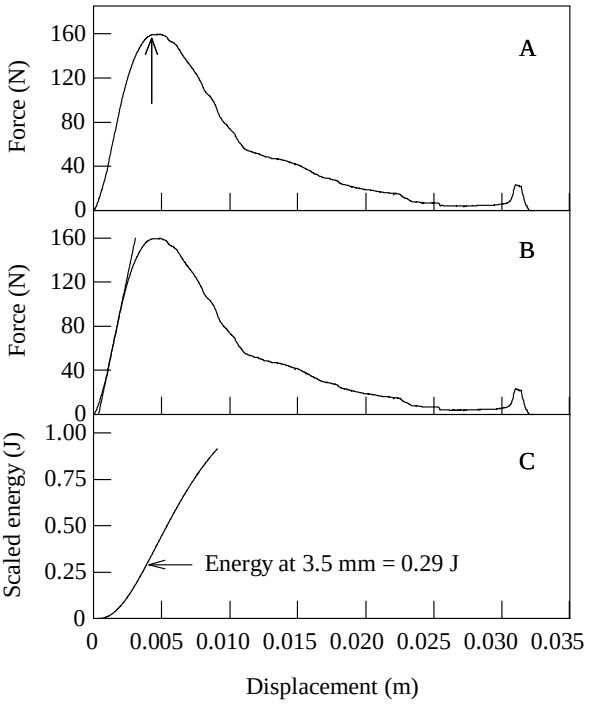

Fig. 3. (A) Typical trace from a CT test ($1.7\times10^{-5}\,m\,s^{-1}$, a=11.65 mm, where a is notch length). The rise in load at the end of the trace was the result of specimen reorientation during the experiment. The arrow indicates the critical point as defined in the text. (B) A linear regression was performed through the initial linear portion of the curve. The inverse slope of this line gave the specimen compliance ($m\,N^{-1}$); the regression line replaced the initial 'toe' of the curve during integration to produce an energy curve which was scaled for a 10 mm thick specimen (C). Zero displacement in C is the intercept of the linear regression and the x-axis in B. The arrow indicates the scaled energy value, which is plotted as a filled symbol in Fig. 5A.

system shown in Fig. 2. To ensure that the Instron reached the desired speed before loading the specimen, the upper clevis mount was slotted to permit 1.5 cm of cross-head travel before the system was engaged. Data from the Instron were fed directly to a computer, where load (kg) and time (s) data were converted to force (N) and displacement (m), respectively (Fig. 3A). The initial low-stiffness (toe) region of the curve was the result of inherent system compliance and was excluded from data analysis by carrying out a linear regression through the linear portion of the curve, extrapolating to the zero load level and using this regression line over the initial nonlinear range (Fig. 3B).

The experimental design for fracture tests at impact loading was similar in principle to that for slower test rates, with the weighted, swinging end of a pendulum providing the energy to move the 'cross-head' (impact T-bar, Fig. 4) at high velocities. A specimen was mounted horizontally in clevis grips; the front and back clevises were attached to a custom-built force transducer and the impact bar, respectively; the latter was supported by a collapsible arm. Specimens were regularly sprayed with distilled water. Displacement was measured with two devices simultaneously: (1) an optical displacement transducer (ODT; Optek Technology Inc., model OPB700; Carrollton, Texas, USA) mounted directly onto the front clevis and (2) a goniometer positioned at the pendulum pivot to provide an indirect measurement of displacement. Displacements recorded from the ODT were used in the first (approximately 25 %) part of the experiment, and goniometer recordings were used for the remaining part when optical measurements became unreliable. The arm of the pendulum was pulled back such that the weighted end was raised by approximately 0.6 m. Force and displacement data were collected with a digital oscilloscope (Data Precision, model Data 6000A) and were transferred to a computer for analysis.

Determination of the J-integral required quantification of a *critical displacement*. This was defined in our study as the point at which any further notch opening resulted in crack propagation. In CT specimens whose notch tip undergoes a large degree of plastic deformation (crack tip rounding) prior to crack propagation, this point is nearly impossible to determine from force–displacement records. Therefore, CT samples fractured at a cross-head rate of $1.7\times10^{-5}\,m\,s^{-1}$ were video-taped during testing to determine an average failure load. The outer face was filmed since crack extension initiates in the outer portion of the SM (M. A. Kasapi and J. M. Gosline, unpublished results). The load at failure was determined by referring to the corresponding load–displacement traces at the point of visible extension of the notch and calculating the failure load as a percentage of maximum load. The maximum

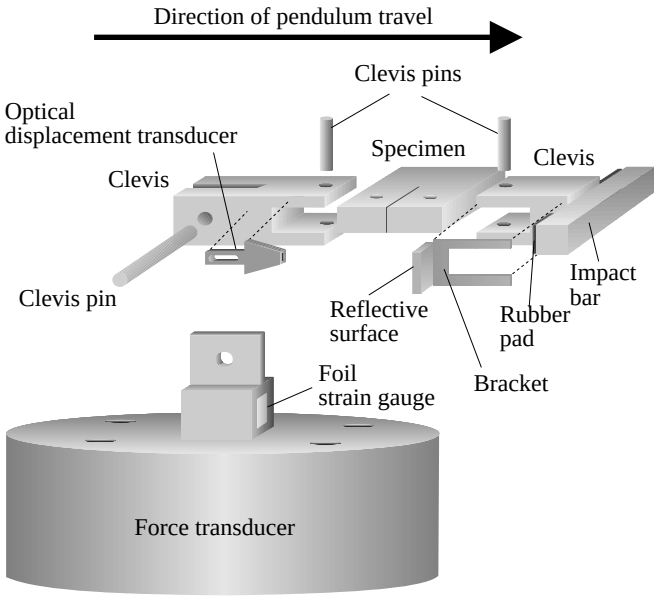

Fig. 4. Exploded diagram of the impact pendulum transducer system. A force transducer was constructed with a foil strain gauge affixed to the front and back of the beam. An optical displacement transducer was mounted to the clevis on the upper left and a white reflective surface attached to a bracket on the upper right clevis. A U-shaped pendulum striker made contact with an aluminium impact bar at the end of the system. Rubber padding was added to dampen resonances.

load was defined as the first peak in load prior to any reduction in the load, regardless of any subsequent increase. This criterion for determining the critical displacement was used for all strain rates.

Each force–displacement record was integrated to an arbitrary point beyond failure to obtain an energy curve (Fig. 3C; specimen thickness varied slightly between samples, therefore energy values were scaled for a 10 mm thick sample). Since samples tested at a particular cross-head rate had different notch lengths, a series of energy curves was produced (one curve for each initial notch length). By finding the scaled energy value at a particular displacement for each sample, a scaled energy *versus* notch length curve was produced (Fig. 5A). A series of these curves was generated at incremental cross-head displacements encompassing all critical displacement values, and a linear equation was fitted to each curve. The *J*-integral was determined by finding the negative value of the slope of the regression line for the critical displacement and dividing by 10 mm. Rather than generating one of these curves for each critical displacement, a function was fitted to the coefficients of these curves (Fig. 5B) to provide an expression which yielded the *J*-integral (after normalization for a 10 mm thick specimen).

The stress intensity factor K was found using the equation provided by ASTM (E399-90):

$$K = [P/(BW^{1/2})]f(a/W)\,, \tag{1}$$

where P is the critical load (N), B is specimen thickness (m), and where:

$$f(a/W) = \frac{(2+a/W)(0.886+4.64a/W-13.32a^2/W^2+14.72a^3/W^3-5.6a^4/W^4)}{(1-a/W)^{3/2}}\,. \tag{2}$$

Initial modulus E_i for CT tests was found by rearranging the equation provided by ASTM (E399-90) for CT specimens under plane strain conditions to obtain:

$$E_i = [(1-\nu^2)/C]q(a/W)\,, \tag{3}$$

where C is the specimen compliance ($m^2\,N^{-1}$) and ν is Poisson's ratio, the ratio of lateral strain to longitudinal strain, and where:

$$q(a/W) = [19.75/(1-a/W)^2]\,[0.5 + 0.192(a/W) + 1.385(a/W)^2 - 2.919(a/W)^3 + 1.842(a/W)^4]\,. \tag{4}$$

The above expression does not contain the thickness term B, since compliance values were already normalized to specimen thickness. Poisson's ratio was estimated to be 0.4 from

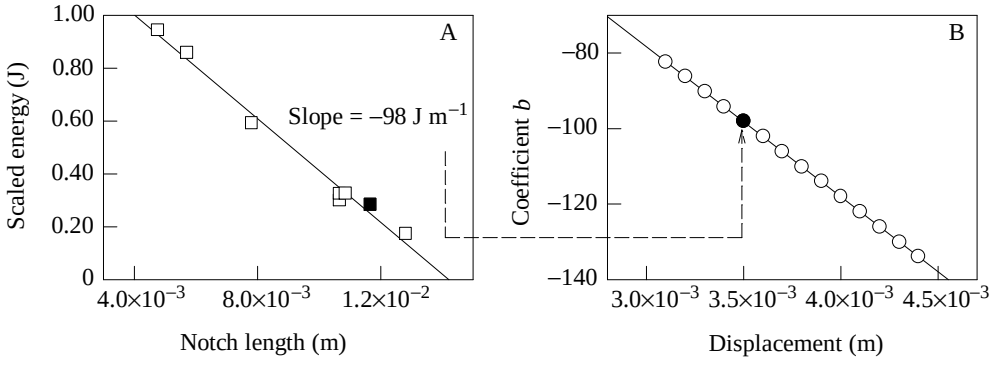

Fig. 5. (A) Energy (scaled for a 10 mm thick specimen) as a function of notch length for the 1.7×10^{-5} m s^{-1} CT tests at 3.5 mm displacement ($y=-98.12x+1.39$, $P<0.0001$, $r^2=0.99$); the filled symbol is the value indicated by the arrow in Fig. 3C. The *J*-integral at this particular displacement would be the negative value of the slope (b) of the regression line, after normalization for a 10 mm thick specimen. A series of these lines was generated at a number of cross-head displacements, encompassing all critical displacement values. (B) Coefficients (or slopes) of these curves were plotted against displacement to provide an expression which yielded the *J*-integral, after normalization for a 10 mm thick specimen ($y=40.8-39708x$, $P<0.0001$, $r^2=1.00$). The filled symbol represents the coefficient from Fig. 5A. Estimates of the *J*-integral can be obtained directly from Fig. 5B by finding the critical displacement on the x-axis, determining the corresponding value of coefficient b and dividing by 10 mm.

preliminary tests that produced values ranging from 0.38 to 0.46.

Tensile tests

Tensile specimens were mounted in the Instron using similar devices as in the CT tests (refer to Fig. 2). Tests were conducted in air so specimens were constantly sprayed with distilled water during longer experiments. Displacement (Δl) values were obtained directly from the specimen by filming the marked reference bar (L_{ref}) (see Fig. 1) using a video camera (Panasonic model WV-BL200) which interfaced with a video dimension analyser (VDA; IPM model 303). Outputs of the Instron and VDA were transferred to a computer where load (kg) and displacement (m) values were converted to stress, σ ($N\,m^{-2}$; $\sigma=F/A_o$ where F is force and A_o is the original cross-sectional area over which the force was applied), and strain, ϵ ($\Delta L/L_o$ where L_o is the length of the marked reference bar in the unloaded condition; mean 25 mm), respectively. Ultimate data were not used from specimens that failed at any area other than the parallel region L_1 of the test specimen.

Owing to the short duration of impact tests, it was not possible to determine strain by filming a reference bar drawn on the specimen. Instead, strain was determined indirectly by measuring the movement of the T-bar (i.e. the cross-head) of the impact apparatus with the ODT and goniometer. A full description of this procedure is outlined in the Appendix.

Resonances were avoided by carefully designing each component of the pendulum system; however, a few resonances remained: the 14 kHz primary resonance of the force transducer, one at approximately 4.1 kHz in CT tests and one at about 2.5 kHz in tensile tests. The lower two resonances were probably generated from resonance of the test specimen at impact. These resonances were present in all respective impact tests, but since test durations were approximately 10 ms and 6 ms for CT and tensile tests, respectively, they could be filtered out quite easily with minimal signal distortion using a fourth-order, zero-phase-shift Butterworth digital filter (Winter, 1990) with 1.0 kHz and 2.0 kHz cut-off frequencies implemented in the software.

A low-pass filter within the Instron limited the frequency response of the system and consequently affected load data from higher test rates (i.e. tests conducted at cross-head rates of 1.7×10^{-3} and $1.7\times10^{-2}\,m\,s^{-1}$) for both CT and tensile tests. Data were corrected using a custom-designed computer program which reversed the filter effect. Displacement data from highest strain rate ($70\,s^{-1}$) tensile tests also required similar correction as a result of the limited frequency response of the VDA system (see Appendix for description of procedures).

Dynamic mechanical tests

Dynamic tests employed a three-point bending test apparatus similar to that previously described by Katz and Gosline (1992). Tests were conducted under distilled water and a downwards pre-load of approximately 30 g was applied to the beams. Small-amplitude vibrations at frequencies ranging from 0.04 to 200 Hz were applied to the beams; the storage modulus E' and the viscous loss function $\tan\delta$ were determined as described previously (Katz and Gosline, 1992).

Results

Tensile and bending parameters

Sample tensile tests for each strain rate are shown in Fig. 6, and mechanical test results are summarized in Table 1. Total energy and maximum stress (σ_{max}) showed a significant increase with increasing strain rate. Although initial modulus E_i rose with increasing strain rate, after a yield region where the slopes of the stress–strain curves showed a rapid drop, the curves had similar slopes. From lowest to highest strain rates, E_i increased about threefold (Fig. 7A), and total energy

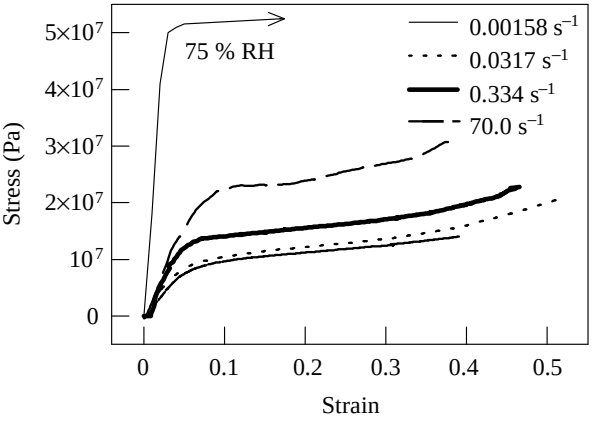

Fig. 6. Typical tensile stress–strain curves for each of the four strain rates used in this study and a representative test at 75% relative humidity (RH) from Bertram (1984). Although the initial modulus rose with increasing strain rate, the shapes of the curves in the post-yield region are similar.

Table 1. *Average initial modulus, total energy, maximum stress and maximum strain for tensile tests at all four strain rates*

Strain rate (s^{-1})	Initial modulus, E_i (GPa)	Total energy ($MJ\,m^{-3}$)	Maximum stress (MPa)	Maximum strain
1.6×10^{-3}	0.28 (4)	5.4 (3)	17 (3)	0.45 (3)
[0.2×10^{-3}]	[0.07]	[1.1]	[3]	[0.05]
3.2×10^{-2}	0.32 (4)	5.6 (3)	19 (3)	0.43 (3)
[0.5×10^{-2}]	[0.05]	[2.3]	[5]	[0.13]
0.33	0.47 (4)	8.5 (3)	25 (3)	0.50 (3)
[0.04]	[0.09]	[1.0]	[2]	[0.04]
70	0.85 (4)	9.7 (2)	30.9 (2)	0.51 (2)
[5]	[0.16]	[0.5]	[0.4]	[0.08]

Values of N are given in parentheses adjacent to mean values; numbers below mean values in brackets are ±1 S.D.

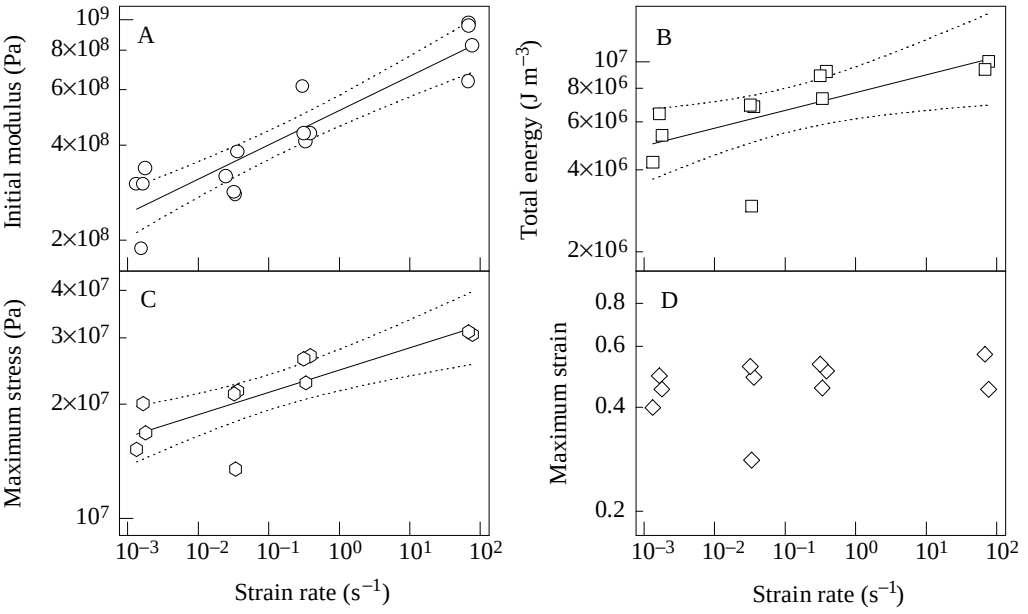

Fig. 7. Tensile test scatter plots of (A) initial modulus E_i ($y=5.15\times10^8x^{0.109}$, $P<0.0001$, $r^2=0.825$), (B) total energy ($y=7.70\times10^6x^{0.0655}$, $P<0.05$, $r^2=0.388$), (C) maximum stress ($y=2.47\times10^7x^{0.0589}$, $P<0.01$, $r^2=0.634$) and (D) maximum strain plotted against strain rate. Although Instron cross-head speed was constant between samples at a specific test rate, strain rate variation in the marked VDA tracking segment caused data points at a particular test rate to deviate slightly on the *x*-axis. Maximum strain was not affected by strain rate (*t*-test; $P>0.05$, $r^2=0.10$). Each point represents one sample; dotted lines are 95% confidence intervals for the regression line.

(Fig. 7B) and σ_{max} (Fig. 7C) rose about twofold. As expected for a viscoelastic material, hoof wall became stiffer with increasing loading rate; however, there was no indication of a transition to brittle behaviour. Instead, the material became stiffer, stronger and capable of absorbing more energy before failure as loading rate increased. There was no statistically significant difference in the mean maximum strain ϵ_{max} (Fig. 7D) with increasing strain rate.

The determination of E_i from CT tests was intended to serve as a validation of CT test methodology. If fracture tests are valid and are conducted on strain-rate-independent materials (e.g. metals), then E_i values from CT and tensile tests should be equal. Although we do not directly compare values from the two tests, Fig. 8A shows that the trends at lower strain rates were similar. Differences in size between tensile and CT samples, and the specific design of CT specimens, made it difficult to assign a particular strain rate to CT tests; however, from lowest to highest cross-head rates, E_i increased twofold. Uncertainty in our CT E_i values as the result of estimating Poisson's ratio is low, as using our highest measured value of 0.46 would lower E_i by only 2.3% and the lowest measurement of 0.38 would raise E_i by 6%. The apparent discrepancy between tensile and CT E_i values at slower strain rates (compare Tables 1 and 2, see Fig. 8A) is probably because smaller CT samples will experience considerably higher strain rates than larger tensile specimens tested at similar cross-head rates. In addition, tensile and CT tests were conducted on specimens obtained from different horses and hence inter-animal variability may be a factor.

Typical data from the middle SM of hoof tested at 75% relative humidity (RH) (Bertram, 1984) are included in Fig. 6 to illustrate the possibility of a continuing trend towards increasing stiffness and maximum stress with increasing strain rate. This comparison is possible because the mechanical

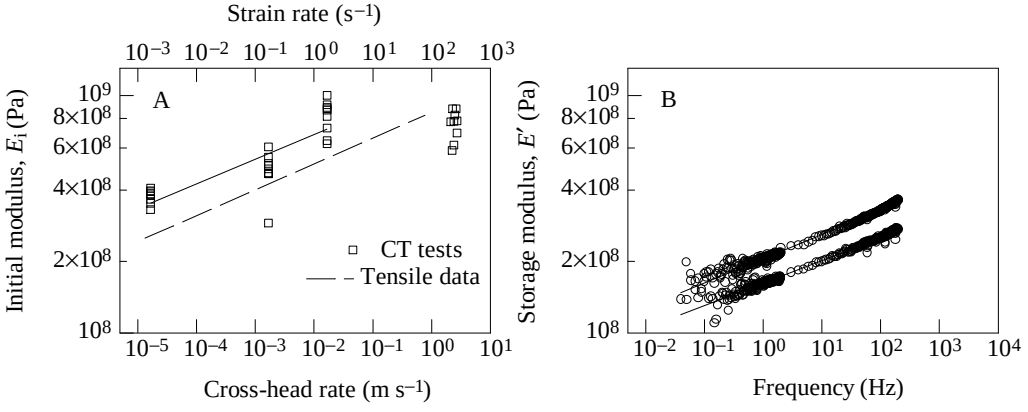

Fig. 8. (A) Scatter plot of initial modulus E_i *versus* cross-head rate for CT tests (squares). The solid regression line ($y=1.10\times10^9x^{0.104}$, $P<0.0001$, $r^2=0.690$) excludes impact data. The regression line from tensile tests (dashed line) is superimposed for comparison. (B) Scatter plots of storage modulus E' *versus* frequency for two three-point bending dynamic tests (regression line for upper data set: $y=2.05\times10^8x^{0.102}$, $P<0.0001$, $r^2=0.988$; regression line for lower data set: $y=1.62\times10^8x^{0.095}$, $P<0.0001$, $r^2=0.920$). Two frequency ranges were tested successively on each beam: 0.04–2 Hz and 1–200 Hz; about 200 points were collected from each range.

Table 2. *Average J-integral, stress intensity factor and initial modulus for compact tension tests at all four cross-head rates*

Cross-head rate ($m\,s^{-1}$)	*J*-integral, *J* ($kJ\,m^{-2}$)	Stress intensity factor, *K* ($MN\,m^{-3/2}$)	Initial modulus, E_i (GPa)	*N*
1.7×10^{-5}	11 (2)	0.71 (0.22)	0.38 (0.03)	8
1.7×10^{-3}	13 (4)	1.0 (0.3)	0.49 (0.09)	9
1.7×10^{-2}	12 (3)	1.4 (0.5)	0.82 (0.13)	9
2.5 (0.3)	12 (3)	1.4 (0.3)	0.76 (0.11)	9

Numbers in parentheses are ±1 S.D.

effects resulting from the removal of a low molecular mass solvent from a polymer–solvent system (e.g. dehydration of proteins) and the effects of increasing strain rate are interchangeable (Ferry, 1980). Therefore, the apparent trend of CT E_i at higher strain rates (Fig. 8A) probably does not represent a true plateau; instead, these CT E_i impact test data could be underestimates as the result of over-smoothing. This is further suggested by the continuing rise in E_i with strain rate seen in both tensile and dynamic tests. Regression exponents for E_i from tensile and CT tests are 0.109 and 0.064, respectively. If impact data in CT tests are excluded from the fit, the new exponent (0.104) is much closer to that obtained from tensile tests. Using the new regression, E_i for impact CT tests should average approximately 1.21 GPa.

Data from two dynamic tests are shown in Fig. 8B. Storage moduli, E', regression exponents (0.102 and 0.095) are indicative of strain-rate-dependence and fall well within the 95 % confidence intervals of Fig. 7A for tensile tests (exponent 0.109). The agreement of modulus trends from three independent strain rate tests and one hydration study (Bertram, 1984) further suggests that a plateau does not exist over the strain rates used in this study and that E_i values from CT impact tests are unreliable. However, the similar trend of CT E_i data from slower tests with that from tensile and dynamic tests indicates that CT methodology is correct.

Direct comparisons between dynamic test data and tensile test data must be carried out with caution. Here, we do not attempt to shift the *x*-axes of the two types of experiment to compare moduli directly since the two *x*-axes differ. If a rough comparison is made, E' values from dynamic tests appear to be lower than E_i values from tensile tests; however, E' is very sensitive to measurement inaccuracies. Inter-animal and inter-sample variability may also contribute to these observed differences.

The viscous loss function $\tan\delta$ averaged 0.145 and was independent of vibration frequency (pooled data *t*-test; $P>0.05$, $r^2=0.003$). This result indicates a constant level of energy loss due to viscous processes over the range of frequencies tested in this study.

Fracture parameters

Stable fracture was observed in all CT tests. A region characterized by a smooth decline in stiffness followed the initial linear region (see Fig. 3). Considerable crack tip rounding and plastic (or pseudo-ductile) deformation were visible in video recordings of the notch front of specimens tested at the slowest cross-head speed. The maximum load usually followed a critical point that signified the start of crack growth. The critical load for CT tests at $1.7\times10^{-5}\,m\,s^{-1}$ was 98.9±0.8 % (mean ±1 S.D.) of the maximum load. Beyond this point, the force–displacement traces became irregular as the initial notch slowly lengthened into a crack and new surfaces were formed.

Fig. 9 shows data from fracture tests. The fracture toughness parameter *J* was unaffected by strain rate (*t*-test; $P>0.05$), suggesting that hoof wall does not pass through a brittle failure transition over the range of strains anticipated *in situ*. Average *J* was $12\pm3\,kJ\,m^{-2}$ (pooled mean ±1 S.D.).

The stress intensity factor *K* followed a trend similar to that of E_i, with mean values doubling from the slowest cross-head rate to impact tests (Fig. 9B). This estimate of fracture toughness implies that hoof wall becomes tougher with increasing test rate. If impact data are excluded from the regression fit, the effect of strain rate is even greater. Neither fracture toughness parameter suggests a compromise in

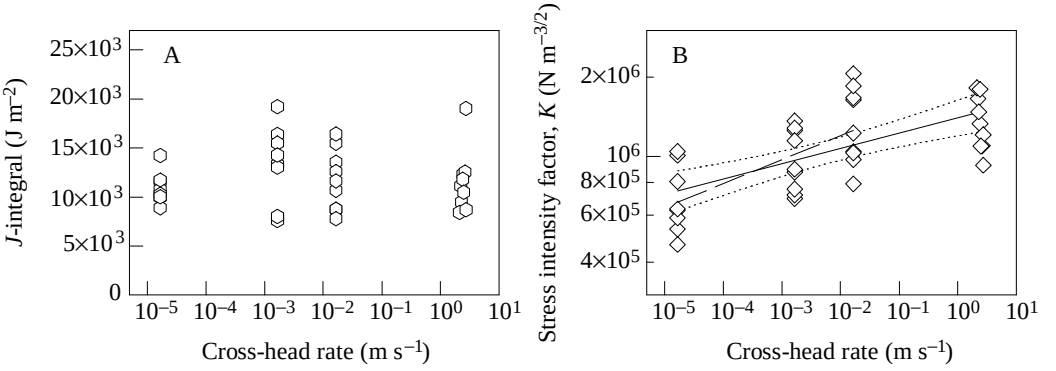

Fig. 9. CT scatter plots of (A) *J*-integral and (B) stress intensity factor *K* ($y=1.40\times10^6x^{0.0578}$, $P<0.0001$, $r^2=0.401$) plotted against cross-head rate for CT tests. *J*-integral was not affected by strain rate (*t*-test, $P>0.05$, $r^2=0.0005$; one-way analysis of variance, $P>0.05$). Each point represents one sample. Dotted lines are 95 % confidence intervals for the regression line. The dashed regression line in B is a fit which excludes impact test data ($y=1.82\times10^6x^{0.0903}$, $P<0.001$, $r^2=0.445$).

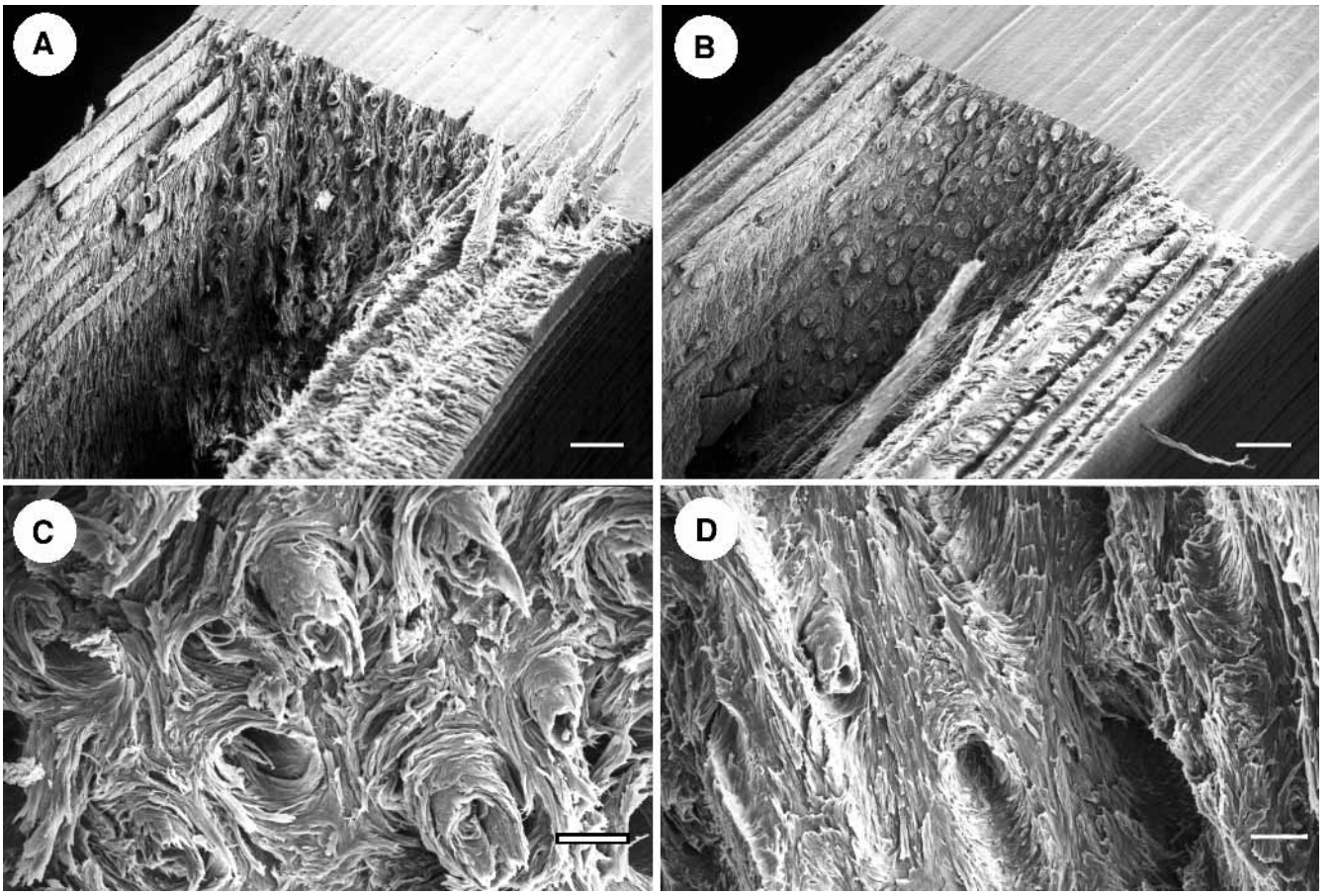

Fig. 10. Scanning electron micrographs of fracture surfaces of specimens tested at the slowest and fastest test rates. (A) Low-magnification (10×) and (C) high-magnification (100×) scanning electron micrographs of fracture surfaces from two samples tested at $1.7\times10^{-5}\,m\,s^{-1}$; (B,D) fracture surfaces of two impact ($2.5\,m\,s^{-1}$) test specimens at the same respective magnifications. Scale bars equal 1 mm in low-magnification and 100 μm in high-magnification photographs. The notched surface appears smooth and is visible in the upper right-hand corner of A and B. Crack growth follows similar patterns at both extreme test rates; the crack followed the tubule axis in outer and inner regions, whereas crack propagation favoured a path at an angle to tubules in the middle region of the stratum medium. Surfaces of impact specimens were much smoother than those tested at slower rate (compare C and D). Curvatures of notch fronts are artefacts created during the dehydration process required for viewing in the scanning electron microscope.

toughness (or a transition to brittle failure) with increasing test rate, contrasting with results from fractography.

Fractography

Scanning electron micrographs (SEMs) of fracture surfaces from two CT specimens conducted at 1.7×10^{-5} and $2.5\,m\,s^{-1}$ are shown on Fig. 10A and Fig. 10B, respectively. The notched surface appears smooth and is visible in the upper right corner of both figures. Curvature of the crack front in Fig. 10B is an artefact of specimen preparation required for viewing in the scanning electron microscope. Surfaces of specimens fractured at impact were generally smoother than those broken at lower strain rates, implying a more brittle mode of failure at impact, but this difference has not been quantified. Crack propagation was generally parallel with tubules and in the plane of the notch in the outer and inner regions of the SM. In these regions, the crack appeared to favour a path along tubule–intertubular 'boundaries', often completely separating tubules and intertubular matrix during fracture. The path of crack growth in the middle region of the SM was dramatically different from that in the inner or outer regions. Cracks characteristically travelled across the tubule axis, apparently following cellular planes of the intertubular material.

Tubule pull-out was evident at all cross-head rates; however, the degree of pull-out was highest in specimens from slowest tests (compare Fig. 10C,D). It was not possible to determine from higher-magnification SEMs whether cracks followed intercellular boundaries or an indiscriminate path through cells and cell interfaces, although fracture surfaces of various textures have been observed, suggesting that cracks travel both through cells and (periodically) along cell-to-cell interfaces. Note, however, that toughness values were obtained just at the (critical) point of crack initiation and that, although surface pattern and texture is consistent in the first few millimetres of crack growth, most of the surface was formed well after the critical point of the experiment.

Discussion

Initial stiffness

The observed rise in E_i with increasing strain rate is indicative of a viscous or viscoelastic material. As strain rate increases, molecular movement becomes more restricted, translating into a higher stress for a given strain. This stiffening will offer the hoof wall increased resistance to deformation during higher speed gaits.

E_i values were generated from CT tests to verify the trend of tensile test E_i with increasing strain rate and to check the validity of fracture toughness calculations using parameters obtained from CT tests. Although data were not directly comparable, the plateau in CT E_i data for impact tests made further testing necessary. Dynamic bending tests were therefore conducted to resolve this issue. These tests also showed a trend of continuing stiffness increase with increasing strain rate, further suggesting that a plateau does not exist. Therefore, impact E_i values from CT tests are probably underestimates of the true values, possibly as a result of data over-smoothing.

The effect of strain rate on E_i over the range tested is not nearly as great as the effect of dehydration. Bertram (1984) found a 36-fold increase in E_i for equine hoof wall tested from 100 % to 0 % relative humidity; our study shows only a threefold increase over five orders of magnitude of strain rate. Bertram's (1984) finding of a continued trend of increasing E_i provides further confidence that a plateau does not exist over our range of test rates.

Ultimate tensile properties and hoof wall viscoelasticity

The observed increase in strength (σ_{max}) with increasing strain rate is also characteristic of viscoelastic materials. As strain rate increases, viscosity rises and large-scale molecular movement is restricted. A larger number of molecular interactions of the viscous, protein–matrix component leads to an increase in the energy absorption of the system. The maximum strain, ϵ_{max}, does not change, as the material apparently fails when molecules become fully extended and covalent bonds are broken. The extension to maximum alignment will therefore be strain-rate-independent. The rise in stiffness and in maximum stress consequently lead to an increase in the total energy input. Using total energy as a measure of toughness, equine hoof wall material appears to become tougher with increasing loading rate; so, as a horse accelerates, increased skeletal loading (Pratt and O'Connor, 1976; Bartel *et al.* 1978; Schryver *et al.* 1978) is met with a concomitant rise in tensile properties, allowing the hoof to absorb more energy before failure.

It is likely that the evolution of the equine hoof wall involved exploitation of the natural mechanical behaviour of viscoelastic solids; the abundance of lipids in the stratum externum probably reflects a need to maintain a certain level of viscosity through hydration. Our material was fully hydrated during all tests, an unusual condition for hoof wall. *In situ*, a gradient of hydration exists in the hoof wall: high to low from inner to outer hoof, and high to low from proximal to distal regions (Leach, 1980). In our study, the outer region of the wall was hydrated to a greater extent above its *in situ* level than the inner region (M. A. Kasapi and J. M. Gosline, unpublished results), and it should be noted that the mechanical effects of viscoelasticity in equine hoof wall peak at an intermediate level of hydration (Bertram and Gosline, 1987).

The mechanical strain-rate-sensitivity observed here for hoof wall keratin has been noted in many other biological materials, including wool (Danilatos and Feughelman, 1979), feather (Bonser and Purslow, 1995), compact bone (Crowninshield and Pope, 1974; Currey, 1975; Carter and Hayes, 1976; Wright and Hayes, 1976; Behiri and Bonfield, 1984; Fisher *et al.* 1986; Evans *et al.* 1992), cranial bone (Wood, 1971), antler (Currey, 1989) and wood (Nadeau *et al.* 1982). The conserved biochemical attributes of hard α-keratin tissues allow generalizations from the small-scale mechanical properties obtained from studies on wool. The viscous components of wool are probably the matrix proteins (Chapman, 1975) intimately associated with water molecules; the fibrous phase appears to contribute the initial elasticity. A mechanical yield region of declining stiffness precedes a post-yield region characterised by a gradual rise in stiffness. Microfibrils (the fibrous phase) are probably responsible for the initial (up to a few per cent strain) linear or Hookean behaviour. Further extension induces a yield resulting from an apparent molecular breakdown of the fibrous phase, whereby a portion of the α-helical fibres are transformed to β-sheet structures (Bendit, 1960). On the basis of data from wool, Feughelman (1994) suggested that this transition is concomitant with a movement of microfibrils closer to one another. Microfibrils eventually displace water molecules such that globular matrix proteins are squeezed by approaching microfibrils. Extension of matrix proteins is believed to be responsible for the increase in stiffness in the post-yield region, irrespective of water content.

As with bone, equine hoof wall consists of numerous levels of structural hierarchy and should not be considered as a simple composite. Comparisons with the mechanical behaviour of simpler keratins (such as wool) must therefore be made with caution. In addition, the tubule–intertubular matrix relationship is not quite analogous to that of a hollow-fibre reinforced composite, as the materials comprising both tubule and intertubular matrix are presumably similar, with only intercellular fibre orientation differing between the two components. Further studies are necessary to determine the mechanical properties of each component and its possible contribution to the hoof.

Hoof wall fracture toughness

To obtain consistent estimates of fracture toughness for a particular material, the sample must be subjected to plane strain (as opposed to plane stress) conditions. Plane strain is a state in which principal strains are confined to one plane (i.e. minimal contraction across the thickness of the specimen). Plane strain conditions occur when specimen thickness B is

greater than $2.5(K_{Ic}/\sigma_y)^2$ (see Broek, 1988), where the subscript Ic represents the critical value of K in mode I loading and y signifies yield. Yield is usually defined as the point of intersection of the stress–strain curve and a line representing some deviation from the initial slope of the curve. Using this criterion for a viscoelastic material is nonsensical because deviation from an initial slope in these materials does not necessarily represent irreversible material change. We may, however, define a yield point for our tests as the stress corresponding to the lowest instantaneous E value. Using this method, the minimum thickness for plane strain conditions in equine hoof wall ranges from about 10 to 11 mm for the highest and slowest strain rates, respectively. Although merely an estimate, this result implies that the condition for plane strain has not been violated in this study. Plane strain conditions are required for testing because toughness values will represent a minimum, conservative estimate of toughness for a particular material (plane stress conditions will inflate fracture toughness). It could, however, benefit an animal to utilize a structure which is thin enough that plane stress conditions exist, yet thick enough to withstand large loads; the equine hoof wall and hoof walls from smaller animals may be designed such that plane stress conditions exist *in vivo* to exploit this phenomenon.

Although our specimens appear to have met the thickness requirement of plane strain conditions, our estimates of the stress intensity factor K must be considered as candidate values, K_Q, and not K_{Ic}. A non-Hookean stress–strain curve eliminates the possibility of determining a reliable value of K_{Ic} and also excludes the use of $K=(EG)^{1/2}$ (see Broek, 1988) to confirm our LEFM results, since an appropriate value of E cannot be determined. However, since K values were determined using the same procedure on all cross-head rates, relative values of K are still useful.

Bertram (1984) reported a value for K of $1.74\,MN\,m^{-3/2}$ for hoof wall tissue tested under similar conditions. This is over twice our value of $0.71\,MN\,m^{-3/2}$ for specimens tested at a comparable rate. This difference could be due to a violation of the conditions for plane strain (his specimens were approximately 3 mm thick) or because only the middle region of the SM was tested. The increase in stress intensity as a function of cross-head rate (Fig. 9B) is expected since K is directly proportional to the critical load P. Since P is sensitive to over-smoothing, as with E_i, K values at impact are also likely to be underestimates. A linear regression fitted to data that excludes impact values provides a coefficient of 0.0903, suggesting that K at impact in CT tests should average approximately $2.0\,MN\,m^{-3/2}$. Using K as a fracture toughness parameter, it appears that equine hoof wall becomes tougher as loading rate increases, a favourable attribute for the horse, since increasing loading rate *in vivo* resulting from a change in gait would probably be concomitant with a rise in load.

Large-scale extensibility coupled with gross crack tip rounding (M. A. Kasapi and J. M. Gosline, unpublished results) suggests that crack propagation is accompanied by extensive plastic deformation in equine hoof wall. For such materials, the use of an LEFM parameter such as G to represent the strain energy release rate is inappropriate. The J-integral technique employed here overcomes the limitations of LEFM in characterising fracture toughness and is therefore a more suitable parameter than G. In addition, J values are probably insensitive to possible errors resulting from over smoothing, as these values were obtained from *relative* changes in energy.

There are, however, limitations with the use of J, and although it is widely accepted as the most versatile single-parameter measure of fracture toughness, our values must still be considered to be estimates. The method in which J was determined used energy differences from specimens with varying notch lengths at the point just prior to stable crack growth. This method assumes self-similarity, whereby the applied notch resembles the cracked surface in both orientation and texture. In our specimens, stable fracture proceeded at an angle to the tubule axis in the middle SM. Fortunately, this pattern was generally observed in specimens at all test rates such that, although absolute values of toughness may not be as accurate as desired, relative values are still valid.

Another required condition which was unavoidably violated with the use of this material was isotropy. Examination of the fracture surfaces in Fig. 10 reveals a ‘recognition’ of the tubular and intertubular components of the hoof wall by the propagating crack and that, at the micro scale, crack progression seems to be sensitive to test rate. That is, the smoother surfaces of impact test specimens imply a less pseudo-ductile and a more brittle behaviour of failure. On the micro scale, path short-cutting should reduce the energy input during fracture as less surface area is created. However, no reduction in energy was statistically evident in our tests; the rise in energy absorption with increasing strain rate (seen in tensile tests) may counter a slightly less pseudo-ductile mode of fracture at higher strain rates, resulting in a constant J value over the range of strain rates tested in this study. Confidence in J may be found with the notch-length-insensitivity of J over the a/W range used (t-test; $P>0.05$ for all tests). This is of paramount importance since if J is to be a valid material parameter, it must represent the toughness of materials regardless of size or shape (within the size limitations discussed earlier). Bertram and Gosline’s (1987) J value of $11.9\,kJ\,m^{-2}$ for middle SM hoof samples tested in a similar manner agrees well with our slower test, verifying the repeatability of these tests.

Using J, our results suggest that there is no effect of strain rate on fracture toughness. In contrast, K implies an increase in fracture toughness with increasing test rate. Recall, however, that K is an LEFM parameter. In linear elastic materials, the stress intensity factor and strain energy release rate will be more tightly coupled, since changes in ultimate stresses will reflect a concomitant change in energy. In viscoelastic materials where the stress–strain curve may be far from linear, the relationship between ultimate load and energy input is often decoupled. By simply representing the critical stress intensity at the crack tip, K ignores the large energy absorption capacity characteristic of many viscoelastic materials. Consequently,

the contribution of crack tip plasticity to fracture toughness (which may be ignored when quantifying the fracture toughness of generally linear elastic materials such as bone), is not recognized by quantifying toughness using K. The J-integral method is more sensitive to the mechanical behaviour of our material and is therefore likely to be a more suitable representation of fracture toughness. Regardless of which parameter is accepted as representing fracture toughness, our results show that toughness is not compromised by the viscoelastic nature of the material at high strain rates.

Functional significance of fractography

To understand the significance of the mechanical properties of a biomaterial, one must consider the use of that material by the organism. Since it is virtually impossible for an organism to produce indestructible materials or structures, some means of repair or replacement is necessary. Unlike bone, which is a living tissue that can undergo adaptive remodelling and repair, the hoof wall is composed of non-living tissue which cannot be repaired. Instead, tissue is continuously generated at the proximal end at a rate of about 1 cm per month (Butler and Hintz, 1977; Buffa *et al.* 1992) to replace an equal amount of material lost distally. The wall must therefore continuously abrade from the distal surface in order to maintain proper hoof shape. It appears that a plane of relative weakness exists parallel with the ground contact surface to provide a crack-diverting mechanism and to allow for necessary wear (Bertram and Gosline, 1986). Fractography of CT specimens agrees with the findings of Bertram and Gosline (1986) for the middle region of the stratum medium, with cracks following a path along the grain of the intertubular material instead of along tubules as one would expect on the basis of the loading conditions of the fracture test. The deviation from this pattern in inner and outer regions is surprising and difficult to explain functionally, although a few possibilities exist.

Three morphologically distinct types of tubules are found in the SM of the equine hoof wall: type I are the innermost and smallest in diameter, type II are the largest and are found between type I and type III tubules, the latter being the outermost tubule type (Leach, 1980). Cells in tubules are thought to be grouped concentrically, forming lamellae of spiralling cortical cells (Nickel, 1938); however, it has also been suggested that the arrangement of cortical cells in bovine hoof more closely resembles the microsporophyll arrangement of pine cones (Wilkens, 1964). Our fracture result suggest that the cellular orientation of the intertubular material in type I and III regions may differ from that previously found for the type II region (Bertram and Gosline, 1986). Alternatively, these regions may have a higher density of tubules, the intracellular fibre orientation of which may determine the fracture path. It may simply be that a plane of weakness is either non-existent in inner and outer regions or that it is not as prevalent as that in the middle region. Tests conducted on specimens isolated from each of these three regions (M. A. Kasapi and J. M. Gosline, unpublished data) suggest that the observed pattern of fracture is not the result of plane stress conditions on the lateral surfaces at the notch front. Further investigation is required to determine whether a plane of weakness exists in inner and outer hoof wall SM.

The overall pattern of crack propagation in CT tests suggest that the hoof wall is designed as a unidirectional, hollow-tubule reinforced ply with no obvious lamellae *per se*. This design forces the crack to follow a more tortuous route than if the crack were to travel in one plane. This process presumably utilizes substantially more energy, making the hoof tougher. Hooves often show surface (type III region) cracks running up the hoof, parallel to the tubule axis. At present, there is no information about the precise three-dimensional orientation of keratin fibres in any region of the hoof wall, the knowledge of which is required for a full understanding of the mechanical properties of this material. Our current research is directed towards the development of a more complete model to explain the mechanical behaviour of this complex, biological composite.

Appendix

Impact tensile test strain determination

To determine strain from impact tensile tests, a pseudo-strain was calculated as cross-head movement divided by the length of the parallel segment L_1 (refer to Fig. 1). Pseudo-strain values were then converted to an estimate of the actual strain by applying a correction factor that was obtained from Instron tests on identical samples in which we measured both pseudo-strain and actual strain. The correction factor from the Instron was applicable to the impact apparatus because their compliances were very similar and because more than 99 % of the total system compliance resulted from deformation of the specimen. Since the slope of the first part of the strain–time curve often differed considerably from that of the rest of the curve, a separate line was fitted through those points used to calculate the initial modulus E_i in Instron experiments. This strain correction factor was used only in calculating E_i for impact tests.

Data correction procedure

The first step in load data correction was characterisation of the Instron filter system. A dual-channel digital spectrum analyser (SA; Wavetek model 5830a) was employed to generate a sinusoidal sweep function from 0 to 10 Hz. This signal was delivered to a Ling V456 electrodynamic vibrator system which acted to load the Instron system through a custom-built reference force transducer. The outputs of the reference transducer and the Instron load cell/electronics were compared by a SA (Wavetek model 5820a) which produced a transfer function for both magnitude and phase between 0 and 10 Hz. 10 Hz was taken as the cut-off frequency since the Instron system acted as a 2 Hz filter and it was decided that five times the filter cut-off frequency would represent the limit of our ability to reconstruct our curve accurately.

A computer program was written to accept a time series and to compute its Fourier transform using the Fast Fourier

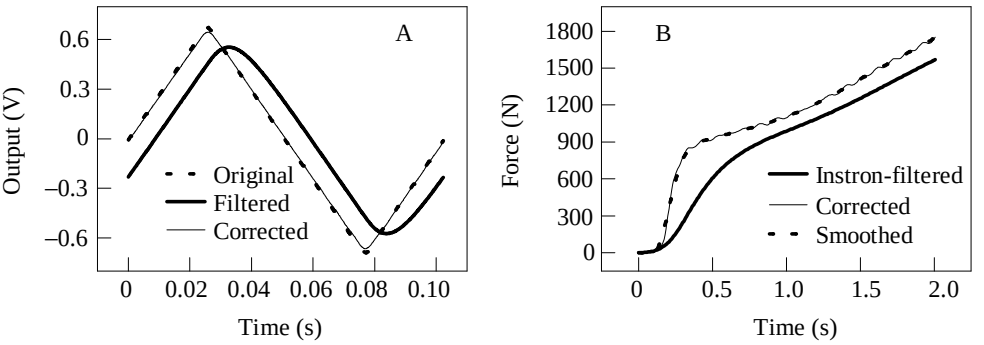

Fig. 11. (A) Test of our data correction program. A 9.77 Hz triangle wave (dashed line) was run through a 40 Hz low-pass filter; the output signal was distorted and phase-shifted (thick, solid line). Data representing the filtered wave were then entered into the computer program which generated a corrected output (thin line). (B) A typical tensile test conducted at $0.33\,s^{-1}$ (thick line). This curve was corrected (thin line) and then smoothed (dashed line) to produce a reliable estimate of the actual event.

Transform (FFT) algorithm (Press *et al.* 1984). The sensitivity of this procedure to the rapid drop in load in tensile tests necessitated the addition of padding to the end of tensile tests. Padding of curves for the $3.2\times10^{-2}\,s^{-1}$ tests involved the addition of the mirror image of the entire curve to the end of the trace; a portion of a sine wave approximating the shape of the force curve was added to the end of $0.33\,s^{-1}$ tests. The transfer function correction factors were applied to the power spectrum and the curve was then reassembled using an inverse FFT. Corrected data were smoothed using a fourth-order digital Butterworth filter (Winter, 1990).

A similar method was used to determine and to correct for the frequency response of the VDA system in Instron tensile tests. Noise was fed into a vibrator motor to which a displacement transducer was affixed. The VDA system was used to follow a marker on the vibrating motor shaft; the outputs of the VDA and displacement transducer were compared by the SA, and the transfer function magnitude and phase were generated. Frequency distortion of displacement data generated from the VDA system was much less than that in force data from the Instron system. Only data from $0.33\,s^{-1}$ experiments required correction, as the result of a minor phase shift.

To test our correction program, we chose an analogous system with controllable parameters. The filter function of a 40 Hz single-pole, low-pass, analog filter was characterised by generating a noise output from an SA and passing it through the filter. The noise generated by the SA was compared with the output of the filter by the SA, and the transfer function magnitude and phase were generated over 200 Hz (i.e. about five times the filter frequency, analogous to our previous method). The reconstruction of a triangle wave was used as a test of our technique, as it was thought to pose a more difficult challenge to our correcting system than our force curves; a 9.77 Hz wave was chosen since this would provide the correction program with about 20 harmonics, the same number of harmonics available for reconstruction of force curves. The triangle wave data were entered into the program and a corrected wave very similar to the original triangle wave was generated (see Fig. 11A).

The FFT technique used in our correction program required that filtered data encompass an entire cycle or some multiple thereof. Fig. 11A shows how well data can be reconstructed when these conditions are met. Our data, however, were not a complete ‘cycle’ and consequently a corrected trace was susceptible to artefacts generated by the program. Force data from $0.33\,s^{-1}$ tensile tests posed the most difficult challenge to our program. A typical force–time curve generated from a $0.33\,s^{-1}$ tensile test is shown in Fig. 11B before and after correction. Here, a low-amplitude, high-frequency ripple is visible on the corrected trace. Addition of the padding described above greatly reduced the amplitude of the ripple generated at the end of the trace such that it was easily filtered out using the Butterworth digital filter.

The authors would like to thank Dr A. Poursartip for his advice and encouragement in the application of fracture mechanics to this study, Mr W. Megill for developing the frequency response correction program and two anonymous referees for constructive comments on the manuscript. This work was conducted while M.A.K. was on a Natural Sciences and Engineering Research Council of Canada Post-Graduate Scholarship.

References

ASTM STANDARD E399-90. (1992). Standard test method for plane-strain fracture toughness of metallic materials. *Annual Book of ASTM Standards*, part 10.

ASTM STANDARD E813-89. (1992). Standard test methods for J_{IC}, a measure of fracture toughness. *Annual Book of ASTM Standards*, part 10.

ASTM STANDARD E8M-90a. (1992). Standard test methods for tension testing of metallic materials. *Annual Book of ASTM Standards*, part 10.

BARTEL, D. L., SCHRYVER, H. F., LOWE, J. E. AND PARKER, R. A. (1978). Locomotion in the horse: A procedure for computing the internal forces in the digit. *Am. J. vet. Res.* **39**, 1721–1727.

BEHIRI, J. C. AND BONFIELD, W. (1984). Fracture mechanics of bone – the effects of density, specimen thickness and crack velocity on longitudinal fracture. *J. Biomech.* **17**, 25–34.

BEHIRI, J. C. AND BONFIELD, W. (1989). Orientation dependence of the fracture mechanics of cortical bone. *J. Biomech.* **22**, 863–872.

BENDIT, E. G. (1960). A quantitative X-ray diffraction study of the alpha–beta transformation in wool keratin. *Textile Res. J.* **30**, 547–555.

BERTRAM, J. E. A. (1984). Fracture toughness design in equine hoof wall. MSc thesis, Department of Zoology, University of British Columbia, BC.

BERTRAM, J. E. A. AND GOSLINE, J. M. (1986). Fracture toughness design in horse hoof keratin. *J. exp. Biol.* **125**, 29–47.

BERTRAM, J. E. A. AND GOSLINE, J. M. (1987). Functional design of horse hoof keratin: the modulation of mechanical properties through hydration effects. *J. exp. Biol.* **130**, 121–136.

BONFIELD, W. (1987). Advances in the fracture mechanics of cortical bone. *J. Biomech.* **20**, 1071–1081.

BONSER, R. H. C. AND PURSLOW, P. P. (1995). The Young's modulus of feather keratin. *J. exp. Biol.* **198**, 1029–1033.

BROEK, D. (1982). *Elementary Engineering Fracture Mechanics*, pp. 115–136. Boston: Martinus Nijhoff Publishing.

BROEK, D. (1988). *The Practical Use of Fracture Mechanics*, pp. 48–122. Boston: Kluwer Academic Publishers.

BUFFA, E. A., VAN DEN BERG, S. S., VERSTRAETE, F. J. M. AND SWART, N. G. N. (1992). Effect of level of feed intake and gelatin supplementation on the growth and quality of hooves of ponies. *J. Anim. Sci.* **44**, 257–261.

BUTLER, K. D. AND HINTZ, H. F. (1977). Effect of level of feed intake and gelatin supplementation on the growth and quality of hooves of ponies. *J. Anim. Sci.* **44**, 257–261.

CARTER, D. R. AND HAYES, W. C. (1976). Bone compressive strength: the influence of density and strain rate. *Science* **194**, 1174–1176.

CHAPMAN, B. M. (1975). The ageing of wool. II. The ageing of disorganized fibers. *J. Textile Inst.* **66**, 343–346.

CROWNINSHIELD, R. D. AND POPE, M. H. (1974). The response of compact bone in tension at various strain rates. *Ann. biomed. Engineering* **2**, 217–225.

CURREY, J. D. (1975). The effects of strain rate, reconstruction and mineral content on some mechanical properties of bovine bone. *J. Biomech.* **8**, 81–86.

CURREY, J. D. (1989). Strain rate dependence of the mechanical properties of reindeer antler and the cumulative damage model of bone fracture. *J. Biomech.* **22**, 469–475.

DANILATOS, G. AND FEUGHELMAN, M. (1979). Dynamic mechanical properties of α-keratin fibers during extension. *J. macromolec. Sci.-Phys.* B**16**, 581–602.

EVANS, G. P., BEHIRI, J. C., VAUGHAN, L. C. AND BONFIELD, W. (1992). The response of equine cortical bone to loading at strain rates experienced *in vivo* by the galloping horse. *Equine vet. J.* **24**, 125–128.

FERRY, J. D. (1980). *Viscoelastic Properties of Polymers*. Toronto: John Wiley and Sons, Inc.

FEUGHELMAN, M. (1994). A model for the mechanical properties of the α-keratin cortex. *Textile Res. J.* **64**, 236–239.

FISHER, R. A., ARMS, S. W., POPE, M. H. AND SELIGSON, D. (1986). Analysis of the effect of using two different strain rates on the acoustic emission in bone. *J. Biomech.* **19**, 119–127.

KATZ, S. L. AND GOSLINE, J. M. (1992). Ontogenetic scaling and mechanical behavior of the tibiae of the African desert locust (*Schistocerca gregaria*). *J. exp. Biol.* **168**, 125–150.

LANDES, J. D. AND BEGLEY, J. A. (1971). The effect of specimen geometry on J_{Ic}. *ASTM STP* **514**, 24.

LEACH, D. H. (1980). Structure and function of the equine hoof wall. PhD thesis, Department of Vet Anatomy, University of Saskatchewan.

LEACH, D. H. (1993). Structural changes in intercellular junctions during keratinization of the stratum medium of the equine hoof wall. *Acta anat.* **147**, 45–55.

MAKINSON, K. R. (1954). The elastic anisotropy of keratinous solids. *Aust. J. biol. Sci.* **7**, 336–347.

MATOLTSY, A. G. (1975). Desmosomes, filaments and keratohyaline granules: their role in the stabilization and keratinization of the epidermis. *J. invest. Dermat.* **65**, 127–142.

NADEAU, J. S., BENNETT, R. AND FULLER, E. R. (1982). An explanation for the rate-of-loading effects in wood in terms of fracture mechanics. *J. Mat. Sci.* **17**, 2831–2840.

NICKEL, R. (1938). Über den bau der Hufröhrchen und seine Bedeutung für den Mechanismus des Pferdehufes. *Morph. Jb.* **82**, 119–160.

PRATT, G. W., JR AND O'CONNOR, J. T., JR (1976). Force plate studies of equine biomechanics. *Am. J. vet. Res.* **37**, 1251–1255.

PRESS, W. H., FLANNERY, B. P., TEUKOLSKY, S. A. AND VETTERLING, W. T. (1984). Fourier transform spectral methods. In *Numerical Recipes: The Art of Scientific Computing*, pp. 381–429. New York: Cambridge University Press.

RICE, J. R. (1968). A path independent integral and the approximate analysis of strain concentration by notches and cracks. *J. appl. Mech.* **35**, 379.

RYDER, M. L. (1962). Structure of rhinoceros horn. *Nature* **193**, 1199–1201.

SCHRYVER, H. F. D. L., BARTEL, N. AND LOWE, J. E. (1978). Locomotion in the horse: Kinematics and external and internal forces in the normal equine digit in the walk and trot. *Am. J. vet. Res.* **39**, 1728–1733.

STEINERT, P. M., MAREKOV, L. N., FRASER, R. D. B. AND PARRY, A. D. (1993). Keratin intermediate filament structure. *J. molec. Biol.* **230**, 436–452.

THOMASON, J. J., BIEWENER, A. A. AND BERTRAM, J. E. A. (1992). Surface strain on the equine hoof wall *in vivo*: implications for the material design and functional morphology of the wall. *J. exp. Biol.* **166**, 145–168.

WILKENS, H. (1964). Zur makroskopischen und mickroskopischen Morphologie der Rinderklaue mit einem Vergleich der Architektur von Klauen und Hufröhrchen. *Zbl. vet. Med.* A **11**, 72–78.

WINTER, D. A. (1990). *Biomechanics and Motor Control of Human Movement*, pp. 36–45. Toronto: John Wiley and Sons, Inc.

WOOD, J. L. (1971). Dynamic response of human cranial bone. *J. Biomech.* **4**, 1–12.

WRIGHT, T. M. AND HAYES, W. C. (1976). Tensile testing of bone over a wide range of strain rates: effects of strain rate, microstructure and density. *Med. Biol. Eng.* **14**, 671–679.